

Bi-global secondary stability theory for high-speed boundary-layer flows

By G. Groskopf[†], M. J. Kloker[†] AND O. Marxen

A finite-difference solver for bi-global secondary linear stability theory is presented and applied to laminar Mach 4.8 boundary-layer flows altered by 3-D “pizza-box” type roughness elements on a flat plate. The steady primary state in flow crosscuts is extracted from accompanying spatial direct numerical simulations (DNS) employing the immersed-boundary technique for the roughness element that is roughly 0.5 undisturbed boundary-layer thicknesses high. A comparison of the stability-theory results past the element with unsteady DNS, where time-periodic perturbations are introduced upstream of the roughness element, shows excellent agreement for the amplitude distribution. The downstream recirculation region and the horseshoe vortex are found to be of minor importance regarding flow destabilization, rather the trailing vortices and the subsequent streaks lead to strong convective shear-layer instabilities in the wake of the roughness element. The 2-D theory helps to verify and validate DNS for this complex flow and allows for efficient stability-parameter scans.

1. Introduction

Over the last decades primary linear stability theory (LST), based on 1-D eigenfunctions over the direction of main shear for downstream traveling waves, has been a reliable tool for investigating the first stage of laminar-turbulent transition in incompressible as well as compressible shear flows with low background disturbance level. On the further way to transition the unstable primary disturbances grow to a weakly nonlinear state, causing a steady wavelike deformation of the shear flow in streamwise direction in a system moving with the wave. Classical secondary linear stability theory (SLST) then provides information on instability with respect to (resonant) spectral secondary disturbances that are similar to the primary waves, however mostly 3-D. SLST is then also an eigenvalue problem with 1-D eigenfunctions, i.e., a monoglobal approach (M-SLST).

Considering compressible boundary-layer flow, the classical M-SLST showed good agreement with temporal DNS in the quasilinear regime of smooth high-speed flows (Pruett *et al.* 1991; Pruett & Zang 1992; Ng & Erlebacher 1992). Compared to spatial DNS, based on the correct physical ansatz for convective instabilities with at first non-unique phase speeds of primary and secondary modes, M-SLST shows severe differences, likely owing to the underlying strong simplifications. Findings of Ng & Erlebacher (1992) could not be confirmed by Eissler & Bestek (1996) and Pruett *et al.* (1996), performing spatial DNS.

The problem of phase speed matching is not present for a baseflow palpably deformed in the spanwise direction. Malik & Chang (1994) and Koch *et al.* (2000) (see also Bonfigli & Kloker 2007) successfully developed an SLST for performing secondary-instability computations for the incompressible case with spanwise crossflow that causes primary

[†] Institut für Aerodynamik und Gasdynamik, Universität Stuttgart, Germany

instability with respect to longitudinal (crossflow-)vortex modes. The primary state with strong crossflow vortices is or can be made steady in a proper reference system and consists now inherently of a spectrum of modes because a crossflow vortex is composed of a multitude of spanwise modes. Strong wall-normal and spanwise gradients exist, and thus, the secondary instability is localized in the flow crosscut rather than monoharmonic. An eigenvalue problem with 2-D eigenfunctions results, i.e., we have a bi-global approach (B-SLST). Recently, Li & Choudhari (2008) started developing a spatial B-SLST code for the investigation of compressible crossflow-dominated swept-wing boundary layers. First computations showed good agreement with experimental data.

In practice, laminar-turbulent transition in high-speed boundary layers is often induced or promoted by discrete 3-D roughness, and even a formally 2-D boundary layer attains steady 3-D deformations by 3-D roughness. Clearly, B-SLST can be used to identify instabilities in the far wake of roughness elements that is dominated by trailing vortices and developing, possibly transiently growing velocity streaks. The same holds for alike situations with effusion cooling (see, e.g., Linn & Kloker 2008). The near-wake region, considered crucially at first due to possible absolute instability, is formally fully 3-D, seemingly demanding a very expensive full, tri-global approach. However, the streamwise gradients typically are still much smaller than the crosswise gradients. Also, in supersonic boundary layers the flow past obstacles undergoes some expansion unlike the incompressible case and thus smaller adverse pressure gradients. Even though 2-D roughness elements may act as a booster to incoming perturbations, their effect typically is not sufficiently strong at higher Mach numbers so that they fail in tripping the laminar boundary layer to turbulence. The modifying mechanisms for disturbance receptivity and instability caused by 3-D elements are still unclear, depending on their shapes, heights, distance, etc. Likewise, the effect of wall cooling can be unexpectedly strong.

Recently, Marxen & Iaccarino (2008) started DNS work at CTR on high-speed boundary-layer transition induced by discrete roughness. The B-SLST can be used for mutual verification and validation with DNS concerning the modified or altered instability that typically leads to accelerated laminar breakdown accompanied by increased wall heating. Moreover, it is a cost-effective additional tool for exploring the stability-parameter space. Very recently, Choudhari *et al.* (2008) also started B-SLST work for the investigation of devices to trip hypersonic laminar boundary layers.

2. Bi-global linear stability theory – governing equations

The bi-global linear stability solver is based on the compressible 3-D Navier-Stokes equations with conservation of mass and energy in gaseous fluid flows, all of them formulated in primitive variables: density ρ , velocity components u , v , w in directions x (streamwise), y (wall-normal), z (spanwise), and temperature T . Neglecting chemical reactions and temperature dependency of specific heat capacities and Prandtl number a calorically perfect-gas flow is assumed at this stage. The velocity components are normalized by u_∞^* (* marks quantities carrying physical units). The density, temperature and viscosity are made dimensionless by their inflow values, and for length scales a reference length L^* is used. Time t and pressure p are non-dimensionalized as follows:

$$t = \frac{t^* \cdot u_\infty^*}{L^*}, \quad p = \frac{p^*}{\rho_\infty^* u_\infty^{*2}}. \quad (2.1)$$

Following the ansatz of LST, all flow quantities are split into their steady primary-state

part Φ_1 and unsteady perturbation part Φ' :

$$\Phi(x, y, z, t) = \Phi_1(x, y, z) + \Phi'(x, y, z, t). \quad (2.2)$$

Furthermore, the following requirements or assumptions apply:

- The general steady primary state $\Phi_1(x, y, z)$ is a solution of the underlying flow equations.
- The employed primary state is assumed to be parallel ($\frac{\partial}{\partial x} \equiv 0$), resulting in a local theory with respect to the main flow direction x , thus

$$\Phi_1 = \Phi_1(y, z). \quad (2.3)$$

This does not imply, in contrast to LST or M-SLST, that $v_1 \equiv 0$ which would eliminate any possibility to investigate vortices in a crosscut plane. The only restriction to be made in spanwise periodic flows is that the mean value or, in spectral space, the zeroth mode of the wall-normal velocity is zero ($\bar{\Phi}$ denotes averaging in z -direction):

$$\bar{v}_1 \equiv 0. \quad (2.4)$$

- Small perturbations are assumed, hence

$$\Phi'_i < 1 \text{ and } \Phi'_i \cdot \Phi'_j \ll 1, \quad (2.5)$$

where the condition for the product holds for any two (i, j) of the flow quantities and their derivatives, respectively, which allows for a linearization.

The linearized perfect-gas equation:

$$\frac{p'}{p_1} = \frac{\rho'}{\rho_1} + \frac{T'}{T_1} \quad (2.6)$$

is used to reduce the number of unknowns replacing p' by ρ' and T' . For the fluid viscosity Eq. (2.2) also holds. The perturbation then can be described by a linearization around the primary state. Hence, using a law only involving temperature dependency (here: Sutherland's law) to model the viscosity yields:

$$\mu = \mu_1 + \mu' = \mu(T_1) + \left. \frac{d\mu}{dT} \right|_{T_1} \cdot T'. \quad (2.7)$$

The spatial derivatives of the viscosity perturbations can be replaced using the temperature perturbations and their spatial derivatives. As thermal conductivity is coupled with viscosity assuming a constant Prandtl number, its primary state and perturbation can be expressed in terms of viscosity.

The last step to be taken in order to obtain the set of stability equations is applying a modal perturbation ansatz:

$$\begin{bmatrix} \rho'(x, y, z, t) \\ u'(x, y, z, t) \\ v'(x, y, z, t) \\ w'(x, y, z, t) \\ T'(x, y, z, t) \end{bmatrix} = \begin{bmatrix} \hat{\rho}(y, z) \\ \hat{u}(y, z) \\ \hat{v}(y, z) \\ \hat{w}(y, z) \\ \hat{T}(y, z) \end{bmatrix} \cdot e^{i(\alpha x - \omega t)}. \quad (2.8)$$

$\hat{\Phi}(y, z)$ is the corresponding complex amplitude distribution of the perturbation in a plane perpendicular to the x -axis, and α and ω describe the spatial wavenumber in x -direction and the frequency, respectively, both of which can be complex. As the second x -derivatives result in terms containing α^2 , a linear eigenvalue problem only results for

the temporal approach ($\alpha = \alpha_r \in R$, $\omega = \omega_r + i \cdot \omega_i \in C$) with the temporal growth rate ω_i :

$$\mathbf{A}_0 \vec{q} + \mathbf{A}_y \frac{\partial \vec{q}}{\partial y} + \mathbf{A}_z \frac{\partial \vec{q}}{\partial z} + \mathbf{A}_{yy} \frac{\partial^2 \vec{q}}{\partial y^2} + \mathbf{A}_{yz} \frac{\partial^2 \vec{q}}{\partial y \partial z} + \mathbf{A}_{zz} \frac{\partial^2 \vec{q}}{\partial z^2} = \omega \mathbf{B} \vec{q}. \quad (2.9)$$

$\vec{q} = \left[\hat{\rho}_{i,j} \hat{u}_{i,j} \hat{v}_{i,j} \hat{w}_{i,j} \hat{T}_{i,j} \right]^T$ is defined as the complex eigenvector of the discretized flowfield, $1 \leq i \leq m$ and $0 \leq j \leq k$ standing for the grid point indices in y - and z -directions, respectively. Thus, every grid point in this plane provides five elements to a total length $L(\vec{q}) = 5 \cdot m \cdot (k+1)$. The square matrices \mathbf{A} of size $L(\vec{q}) \times L(\vec{q})$ represent the coefficients of the corresponding derivatives of the unknown perturbation amplitudes. \mathbf{B} has the same size and is the matrix of coefficients directly bound to the eigenvalue ω .

The flowfield is discretized using finite differences (see Sec. 3.1). Therefore, any derivative of \vec{q} can be described as a matrix-vector product of the corresponding finite-difference coefficient matrix \mathbf{D} and \vec{q} itself, as, e.g., for the first derivative in wall-normal direction:

$$\frac{\partial \vec{q}}{\partial y} = \mathbf{D}_y \vec{q}. \quad (2.10)$$

\mathbf{D}_y again is of size $L(\vec{q}) \times L(\vec{q})$. Thus it is possible to isolate \vec{q} and to convert Eq. (2.9) into a generalized eigenvalue problem:

$$\mathbf{A} \vec{q} = \omega \mathbf{B} \vec{q}, \quad (2.11a)$$

with

$$\mathbf{A} = \mathbf{A}_0 + \mathbf{A}_y \mathbf{D}_y + \mathbf{A}_z \mathbf{D}_z + \mathbf{A}_{yy} \mathbf{D}_{yy} + \mathbf{A}_{yz} \mathbf{D}_z \mathbf{D}_y + \mathbf{A}_{zz} \mathbf{D}_{zz}. \quad (2.11b)$$

Building the whole matrices, the solver would be capable of extracting the complete spectrum of eigenvalues but would also require tremendous computational resources. Therefore an iterative method is used to gain only parts of the eigenvalue spectrum.

3. Numerical method

3.1. Discretization

As the theory is localized with respect to the downstream direction, every (y - z)-crosscut plane is investigated independently. This plane is discretized by a Cartesian grid (for straight walls) allowing for arbitrary grid refinement or stretching in both directions. A mapping onto an equidistant computational grid via metric terms included in the equations is used. In both directions principally eighth-order central finite-differences (FDs) are used for the first and second derivatives of the primary state. Near boundaries in wall-normal direction, central sixth- and fourth-order and eventually biased FDs of at least fourth order are employed. The spanwise direction is assumed periodic and not symmetric within a periodicity unit, thus the full domain is covered by central FDs. They just reach over to the other side of the domain. The same FDs are used for the coefficient matrices that couple the flow perturbations with their derivatives, see Eq. (2.10).

Using FDs, also non-periodic primary states can be considered, a feature planned to be used in future work. If the given primary state is not periodic but symmetric in spanwise direction, a simple adaptation procedure is employed. The corresponding vertical grid lines at the (y - z)-plane's lateral edges are duplicated and repeatedly attached to both edges. The flow quantities on the added grid lines finally are filtered in spanwise direction using a second-order approach to remove possibly induced high wavenumber modes.

This way it is ensured that the FDs of first and second spanwise derivatives give zero for all flow quantities at the spanwise boundaries of the computational domain. This procedure can also be applied to primary states with a large spanwise periodicity length. From such flows a section exhibiting the significant flow structures can be extracted and analysed with significantly reduced computational cost. For an example see the report by Birrer *et al.* (2008) in this book. A careful check of the results with respect to the added side regions is then performed to ensure a minimized interaction of the “pseudo-periodic” flow structures, and thus, irrelevance for the instability results.

3.2. Boundary conditions

The primary-state flow is periodic in spanwise direction. The same behavior holds for the perturbations with the same periodicity length for fundamental disturbances. Bonfigli & Kloker (2007) and Wassermann & Kloker (2005) convincingly explained that spanwise subharmonic disturbances do not need to be considered for the setup studied here.

At the wall and at the freestream we force Dirichlet conditions for the perturbations. (For the freestream boundary also an exponential decay (von-Neumann-type) condition could be used as in our incompressible-LST work, where it enabled a much smaller integration-domain height. However, first tests did not lead to unambiguous results for the B-SLST case.) Therefore, the equations do not have to be solved for these grid points. In order to keep the grid definitions made above, the indices 0 and $m + 1$ are assigned to the wall and the upper edge of the computational domain, respectively.

At the wall the no-slip condition is prescribed, setting the perturbations of the velocity components to zero. The same holds for the temperature perturbation:

$$\begin{aligned} \hat{u}_{0,j} &= 0 \\ \hat{v}_{0,j} &= 0 \\ \hat{w}_{0,j} &= 0 \\ \hat{T}_{0,j} &= 0. \end{aligned} \tag{3.1}$$

In the freestream, high enough above the shear layer, all perturbations are assumed to vanish:

$$\begin{aligned} \hat{\rho}_{m+1,j} &= 0 \\ \hat{u}_{m+1,j} &= 0 \\ \hat{v}_{m+1,j} &= 0 \\ \hat{w}_{m+1,j} &= 0 \\ \hat{T}_{m+1,j} &= 0. \end{aligned} \tag{3.2}$$

3.3. Method for solving the eigenproblem

As mentioned in Sec. 2 the code is in principle capable of calculating the full eigenvalue spectrum of the problem, e.g., by using an algorithm based on the QR method. But this is only workable for small-size problems, and therefore is only used to get an overview of the full spectrum with a relatively low resolution.

When confronted with large-scale eigenvalue problems it is advisable to switch to an iterative method providing only parts of the spectrum but having the potential to significantly reduce the needed computational time. This especially holds if the region of interest within the spectrum is known or can be narrowed down to only contain a low percentage of the complete set of eigenvalues. On the other hand, this approach allows for enhanced resolution for the investigated crosscut plane.

The algorithm applied here is the implicitly restarted Arnoldi method (IRAM) implemented in a collection of Fortran subroutines called ARPACK and designed to solve large-scale eigenvalue problems. For complex generalized eigenvalue problems

$$\mathbf{M}\vec{x} = \lambda\mathbf{N}\vec{x} \quad (3.3)$$

there are standard options to find eigenvalues of largest/smallest real or imaginary part and largest/smallest modulus. However, in the problems faced in this investigation the eigenvalues of interest may not be the ones at the boundaries of the spectra but interior ones. These can be isolated using the Shift-and-Invert mode, which computes the specified number of eigenvalues in the vicinity of a specified point σ in the complex plane, transforming Eq. (3.3) to

$$(\mathbf{M} - \sigma\mathbf{N})^{-1} \mathbf{N}\vec{x} = \nu\vec{x} \quad \text{where} \quad \nu = \frac{1}{\lambda - \sigma}. \quad (3.4)$$

This way the eigenvalues λ_l near σ are shifted to eigenvalues ν_l at the outer boundary of the transformed spectrum. Hence, computing the eigenvalues ν_l of largest modulus and transforming them back yields the interior eigenvalues λ_l in the requested region of the complex plane. The corresponding eigenvectors are not affected by the transformation and remain unchanged. For details, see Lehoucq *et al.* (1998).

The ARnoldi PACKage provides a so-called reverse communication interface, telling the user when interaction with the ARPACK routine is required. This interaction simply comprises the actions of taking an intermediate result vector provided by the ARPACK routine, performing the requested action of the matrix to the specified vector, e.g., solving the linear system $(\mathbf{M} - \sigma\mathbf{N})\vec{x} = \vec{b}$ for \vec{x} , and handing back the result to the routine starting the next iteration step. The iteration stops when the requested number of eigenvalues and/or the corresponding eigenvectors with the requested tolerance have been found.

3.4. Computational cost

In its current version the solver stores the full matrix \mathbf{A} of complex values requiring 60GB of RAM for the whole computation with a typical resolution of 6764 grid points ($m = 89$, $k = 75$) resulting in a matrix size of $L(\vec{q}) \times L(\vec{q}) = 33820^2$ ($\approx 1.14 \cdot 10^9$ matrix elements). However, as this matrix is sparse with few non-zero elements, there is a storage-requirement reduction potential of more than 99% for the matrix if it is built in a sparse-matrix format like the Compressed Column Storage (CCS), which only stores the non-zero elements and their corresponding coordinates within the full matrix.

Generally, the computing time needed to extract a part of the eigenvalue spectrum is not only a matter of resolution but also is strongly dependent on the number of eigenvalues to be determined as well as the structure of the spectrum. The IRAM is a rather fast algorithm if the demanded eigenvalues are isolated in their position in the complex plane or part of a cluster which is fully resolved. In contrast, splitting such a cluster in the sense of only calculating some, not all, of the included eigenvalues slows the algorithm down. As the structure of the spectrum is hard to be foreseen, depending on the flowfield as well as on the computational grid, it is hard to avoid these decelerating aspects. A promising approach to this problem is the parallelization of the solver. For the current version running on one processor of an NEC SX-8 vector-computer node, the average computing time for the determination of a partial eigenvalue spectrum of the flowfield crosscuts discussed here, including the corresponding eigenfunctions for the typical resolution described above, is approximately 3.5 hours. This time will be decreased by parallelization as well as optimization of the furthermore required matrix-vector op-

h_R	L_R	s_R	$x_{c,R}$	α_S	β_S	ϱ_1^2	ϱ_2^2	ϱ_3^2
0.1	0.4	20.0	15.0	10^5	$5 \cdot 10^3$	$1 \cdot 10^{-4}$	$5 \cdot 10^{-5}$	$1 \cdot 10^{-4}$

TABLE 1. Coefficients to define the shape of the roughness and parameters used in the immersed boundary method.

erations. The optimization concerning storage requirements as well as computing time consumption currently is in progress.

4. DNS method for primary states

The basis for the numerical method to compute the primary-state flow is an algorithm described in Nagarajan *et al.* (2003). Solutions to the compressible Navier-Stokes equations (written in non-dimensional form) are obtained, applying sixth-order compact finite-differences together with explicit Runge-Kutta time-stepping of third order. The numerical discretization is constructed on a structured, curvilinear grid using staggered variables. Second derivatives are computed by applying the first derivative twice, but due to the staggering the accuracy is equivalent to a direct computation. A shock-capturing scheme was not required as occurring shocks were very weak and could be treated by applying a high-order compact numerical filter.

A roughness element is placed on a flat plate. This element is handled by an immersed boundary method (IBM), following an approach described in Mittal & Iaccarino (2005) and von Terzi *et al.* (2001). A volume-forcing term B_i of the following form is added to the r.h.s. of the momentum equations ($\vec{x} = (x \ y \ z)^T = (x_1 \ x_2 \ x_3)^T$):

$$B_i(\vec{x}, t) = \rho \oint_S b_i(\vec{x}_S) \cdot g(\vec{x} - \vec{x}_S) dS, \quad (4.1)$$

$$\text{with } b_i(\vec{x}_S, t) = \alpha_S \cdot \int_0^t u_i(\vec{x}_S, t') dt' + \beta_S \cdot u_i(\vec{x}_S, t) \quad (4.2)$$

$$\text{and } g(\vec{x} - \vec{x}_S) = \Pi_{i=1\dots 3} \exp\left(-((x_i - x_{i,S})/\varrho_i)^2\right). \quad (4.3)$$

The coefficients in Eqs. (4.1)–(4.3) are given in Table 1. The determination of all the geometrical information required to enforce the immersed boundary, i.e., setting of \vec{x}_S , is carried out in a pre-processing step. The shape of the roughness $\vec{x}_S = (x \ y_w \ z)^T$ is defined by the following analytical function:

$$y_w(x, z) = h_z(z) \cdot (\tanh(s_R(x - (x_{c,R} - L_R/2))) - \tanh(s_R(x - (x_{c,R} + L_R/2)))) , \\ \text{with } h_z(z) = h_R/4 \cdot (\tanh(s_R(z + L_R/2)) - \tanh(s_R(z - L_R/2))) , \quad (4.4)$$

where y_w specifies the distance from the surface of a plate without roughness. The coefficients appearing in this equation are specified in Table 1. The IBM has shown very satisfactory agreement for both mean flow and small perturbations if compared to solutions using a body-fitted grid for a 2-D roughness (Marxen & Iaccarino 2008).

Freestream parameters are the same as in Marxen & Iaccarino (2008) and are given in Table 2. Compared to Marxen & Iaccarino (2008), the inflow is moved downstream and the outflow upstream so that the integration domain is only half as long. Spanwise periodicity is forced, but no symmetry. The origin of the coordinate system is located at the leading edge of the flat plate. The grid is uniformly spaced in streamwise direction

Re	Pr_∞	Ec_∞	M_∞	\tilde{T}_∞	x_{ifl}	x_{ofl}	y_{bot}	y_{top}	NX	MY	KZ
10^5	0.71	1	4.8	55.4 K	9.996	24.776	0	1.575	400	200	40

TABLE 2. Overview of simulation parameters, domain size and resolution.

x (NX points) and in the periodic spanwise direction z (KZ points). In wall-normal direction y (MY points), a grid stretching is applied as detailed in Marxen & Iaccarino (2008).

At the inflow x_{ifl} , a self-similar solution is prescribed while the wall boundary condition (B.C.) at y_{bot} is adiabatic with a no-penetration and no-slip condition. Within a certain region close to the outflow x_{ofl} and in the freestream y_{top} , the solution is damped toward the laminar self-similar solution.

We note that the stability results rely on the primary state, demanding a careful temporal as well as spatial convergence study in computing the primary flowfield. The (x - y)-grid was found sufficient for 2-D roughness elements but grid studies still need to be done for the 3-D roughness elements. 36,000 time steps ($\Delta t = 10^{-3}$) have been computed for the cases considered here. This corresponds to a physical time of about 1.5 ms, based on a total pressure $p_0^* = 1$ bar. In the temporal evolution the flows show reasonable convergence in terms of alterations in the stability results. With increasing time, the maximum instability growth decreases from values that are too large because the vortices/streaks get weaker while reaching their final structure. However, a fully converged steady state is not yet reached. Furthermore, wavelike (varicose) structures traveling downstream can be observed. Temporal evolution of the flow indicates that these are convective, originating from the start of the computation, leaving the computational domain when a sufficiently high number of time steps has been computed. Using the current state of the computation the primary state has been time averaged over the last 1200 steps corresponding to one period of the frequency $\omega = 2\pi f = 5$.

5. Results

5.1. Investigated configurations

The configuration under investigation is an adiabatic flat-plate boundary-layer flow carrying pizza-box type roughness elements in a cold, supersonic flow. The freestream has a Mach number $Ma_\infty = 4.8$, the temperature is $T_\infty = 55.4$ K resulting in a total temperature $T_0 = 311$ K. Therefore, the calorically perfect-gas flow is a legitimate assumption. Prandtl number and adiabatic exponent are fixed to 0.71 and 1.4, respectively. The Reynolds number based on the reference length L^* is $Re = 10^5$, thus $\rho_\infty^* L^* = 4.87 \cdot 10^{-4} \frac{kg}{m^2}$ with $\mu_\infty^* = 3.49 \cdot 10^{-6} \frac{Ns}{m^2}$ and $u_\infty^* = 716.15 \frac{m}{s}$.

For the roughness elements, two major mounting configurations are investigated. In both cases the elements are placed at $x = 15.0$ downstream of the leading edge of the plate, corresponding to $R_x = 1225$, with a height h of 0.55 boundary-layer thicknesses of the unperturbed flow δ_u at that position. The difference between the two major configurations is the angular setting with respect to the oncoming flow, Fig. 1. In Case I, referred to as “square” or “blunt” case, the pizza box faces the flow with one side. In Case II, named “diamond” or “sharp” case, the box faces the flow with a corner.

In Case I the box edge is set to $e = 2.2\delta_u$. The same holds for Case IIa. But rotating the element increases its width b perpendicular to the incoming flow by a factor of $\sqrt{2}$,

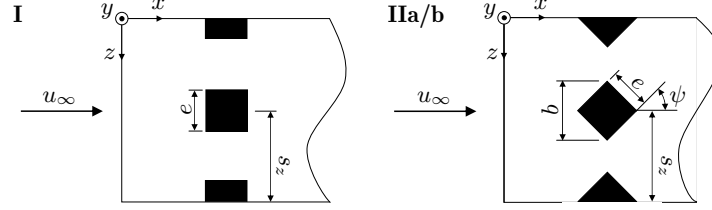


FIGURE 1. Sketch of the investigated roughness settings. Case I: “blunt” pizza box of width e and spanwise spacing s_z , Cases IIa/b: “sharp” diamond box.

Case	e	b	s_z/b	h	ψ
I	$2.2\delta_u$	$2.2\delta_u$	3.0	$0.55\delta_u$	0°
IIa	$2.2\delta_u$	$2.2\sqrt{2}\delta_u$	2.1	$0.55\delta_u$	45°
IIb	$1.1\sqrt{2}\delta_u$	$2.2\delta_u$	3.0	$0.55\delta_u$	45°

TABLE 3. Overview of “pizza-box” settings for the investigated cases. Symbols refer to Fig. 1.

and thus alters the area blocking the flow. Therefore, Case IIb is a box scaled down by $1/\sqrt{2}$ to have the width b of Case I. This way it is possible to discern the two different effects of varying the element’s angular bearing and increasing the blocking area to the flow. An overview of the investigated configurations is given in Table 3.

5.2. Steady primary states

Figure 2 shows a top view of the primary-state flowfields of all three cases. Isosurfaces of the λ_2 -criterion indicating vortices are shown. The shading describes the height y above the wall. Furthermore, the dimensions of the recirculation zones in front of and behind the roughness element are displayed. Two pairs of counter-rotating vortices (CVPs) can be observed. The velocity isolines in Fig. 3 indicate the rotation direction of the inner vortex pair. Between them low-momentum fluid is lifted up toward the boundary-layer edge, forming a low-speed streak behind the element. This is contrary to the high-speed streaks, often observed behind a roughness element in subsonic flow, generated by a horseshoe-type vortex.

Downstream of $x = 16.0$ the vortex patterns of all cases seem to be roughly similar in form and magnitude of vorticity as well as lift-up. Generally, the lift-up of vortices in streamwise direction additionally increases the shear near the boundary-layer edge providing the base for increased instability. However, in the three cases discussed here the opposite effect of decreased shear resulting from the boundary-layer growth apparently exceeds the lift-up effect, leading to an overall decay of $\frac{\partial u}{\partial y}$ in the far wake.

Nonetheless, there are obvious differences in spanwise spacing of the vortices and in their formation right behind the roughness element. Comparing IIb to the other cases

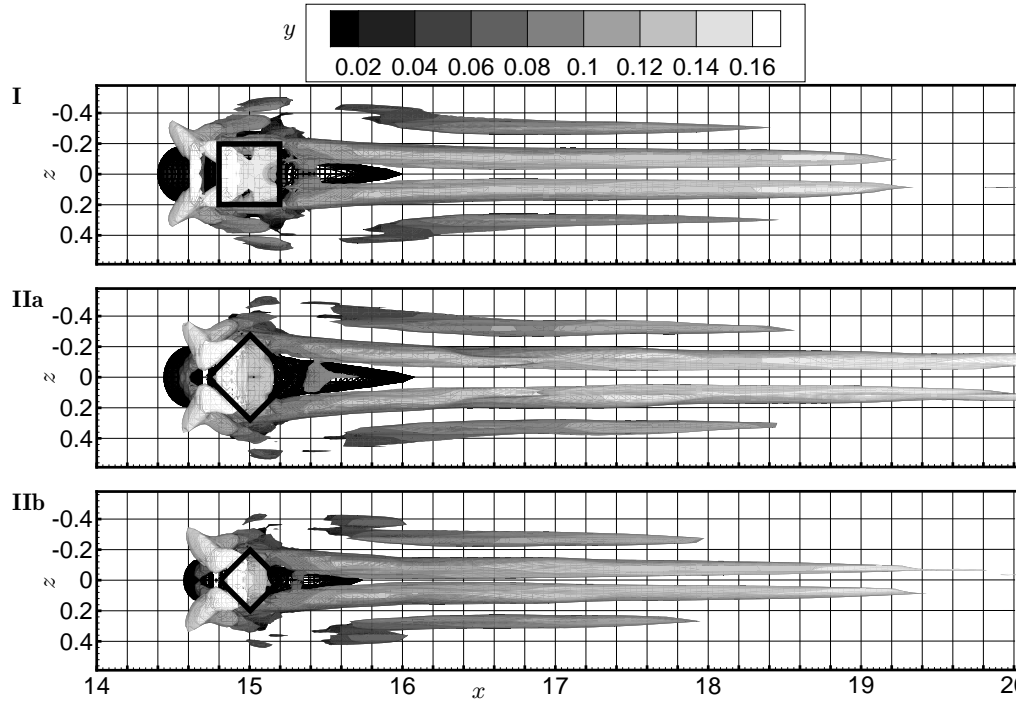


FIGURE 2. Top view of vortex structures in the wake of the roughness element for the three investigated configurations, visualized by means of the λ_2 criterion ($\lambda_2 = -0.04$). The shading indicates the height y of the λ_2 -isosurface above the wall. The meshed isosurface shows the dimension of the recirculation zones ($u < 0$). Thick solid lines show the borders of the roughness elements.

reveals that the spanwise spacing of the inner CVP is much smaller, indicating that in Case IIb the wall-normal and spanwise gradients are more localized although similar in distribution (see Fig. 3). Owing to the closely situated vortices, the velocity gradients are larger initially (see Fig. 4).

The maximum discrepancy in the wall-normal u -velocity gradients is found in the near wake at about $15.5 \leq x \leq 17.0$. Compared to Cases I and IIa the maximum of the wall-normal gradient for Case IIb roughly is 16% larger. However, the differences disappear with increasing streamwise distance. The same holds for the spanwise gradient, just at lower absolute values. Generally, it can be observed that the wall-normal gradient diminishes with streamwise distance behind the roughness element while the maximum spanwise gradient persists. This indicates the decay of vorticity, supported by the visualization in Fig. 2 showing the weakening and vanishing of the CVP that is accompanied by the formation of spanwise velocity streaks.

Another differing feature influencing the formation of the CVPs is the recirculation zone. As can be seen in Fig. 2 for Cases I and IIa, the flow reversal behind the roughness element extends across a similar length while for Case IIb it is much shorter. On the other hand, the “diamond” Cases IIa and IIb have in common that the inner vortices seem to form aligned to the recirculation zone (to be seen in top view, Fig. 2), being curved and therefore diminishing their initial spanwise spacing, while in Case I the curvature is less pronounced resulting in a larger gap between the inner vortices in the far wake for

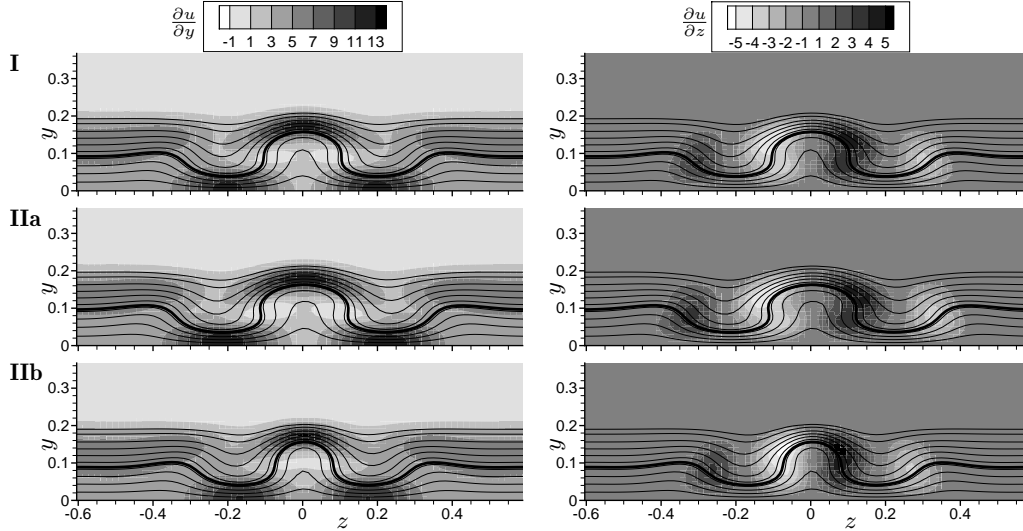


FIGURE 3. Contours of wall-normal (left) and spanwise (right) gradient of u -velocity at $x = 18.0$ for the three investigated cases. Thin solid lines are isolines of u beginning with $u = 0.1$ near the wall and ending with $u = 0.95$. Thick solid lines mark the sonic line.

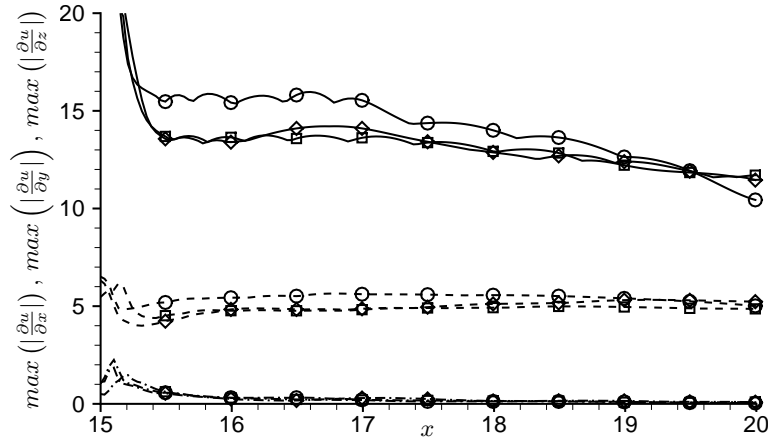


FIGURE 4. Maximum of absolute values of wall-normal (solid lines), spanwise (dashed lines) and streamwise (dash-dot lines) u -velocity gradients in $(y-z)$ -planes over streamwise direction x . Case I: squares, Case IIa: diamonds, Case IIb: circles.

the same element width b . The horseshoe-type vortex forming in front of each roughness element is at first not much closer to the wall, but downstream it lies below the CVP. Its rotation sense is opposite to the CVP's sense. The white horns in front and above the roughness indicate compression-/shock-induced vorticity regions.

In Fig. 4 the run of the $\frac{\partial u}{\partial y}$ curves in the near wake ($15.5 \leq x \leq 17$) shows characteristics of wavelike behavior. This was not observed at earlier time stages. The origin is unclear, and the further temporal evolution has to be investigated. Remaining in space (in the near wake of the roughness element) and growing with time this behavior could indicate

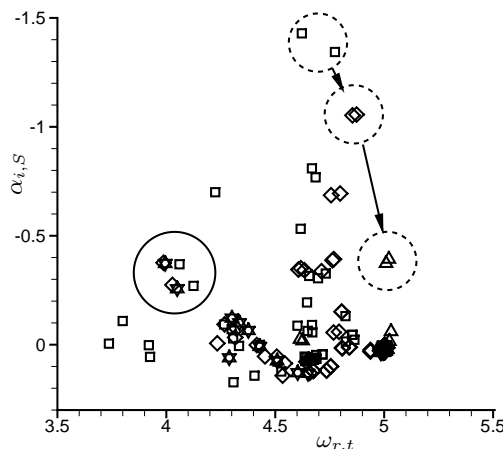


FIGURE 5. Parts of the eigenvalue spectrum for Case I at $x = 18.0$ for increasing spanwise resolution. Squares: 40 points in z , diamonds: 76 pts., deltas: 104 pts., gradients: 142 pts. $\alpha_{i,S}$ is determined using Eq. (5.1). Dashed-line circles indicate the evolution of a numerical-eigenvalue pair with increasing spanwise resolution (arrows). The solid-line circle shows the most amplified pair of physical eigenvalues.

absolute instability, albeit of rather low growth. As a combined temporal and spatial stability solver is not yet available absolute instabilities are not considered here.

$\frac{\partial u}{\partial x}$ is included in Fig. 4 to justify the assumption of parallel flow which allows for the application of the bi-global stability theory.

5.3. Stability analysis

The bi-global linear stability analysis is carried out in $(y-z)$ -crosscut planes at different downstream positions in the wake of the roughness element. From the obtained spectrum the most amplified physical eigenvalues and their corresponding eigenfunctions are isolated. Figure 5 shows parts of the spectrum for different spanwise resolutions. At low spanwise resolutions the most unstable modes are numerical/unphysical, and can be identified by wiggly eigenvector-phase distributions already for the lowest resolution case. Increasing the spanwise resolution the amplification rate of these modes decreases until they vanish from this part of the spectrum at all. The most amplified physical eigenvalues undergo only minor improvements by increasing the resolution, however, to secure their physical relevance, grid studies are necessary.

As the stability approach is temporal (index t), yielding frequency $\omega_{r,t}$ and temporal amplification rate $\omega_{i,t}$ for a given streamwise spatial wavenumber $\alpha_{r,t}$, the amplification rates $\alpha_{i,S}$ for the spatial approach (index S) are obtained applying Gaster's transformation according to Koch *et al.* (2000), see also Bonfigli & Kloker (2007):

$$\begin{aligned} \omega_{r,S} &= \omega_{r,t} \\ \alpha_{r,S} &= \alpha_{r,t} \\ \hat{\Phi}_S(y, z) &= \hat{\Phi}_t(y, z) \\ \alpha_{i,S} &= -\frac{\omega_{i,t}}{c_{gr,t}}, \quad c_{gr,t} = \frac{\partial \omega_{r,t}}{\partial \alpha_{r,t}} \approx \frac{\omega_{r,t}}{\alpha_{r,t}} = c_{ph,t}. \end{aligned} \quad (5.1)$$

Two different instability modes are shown. Called y -(or even) mode and z -(or odd)

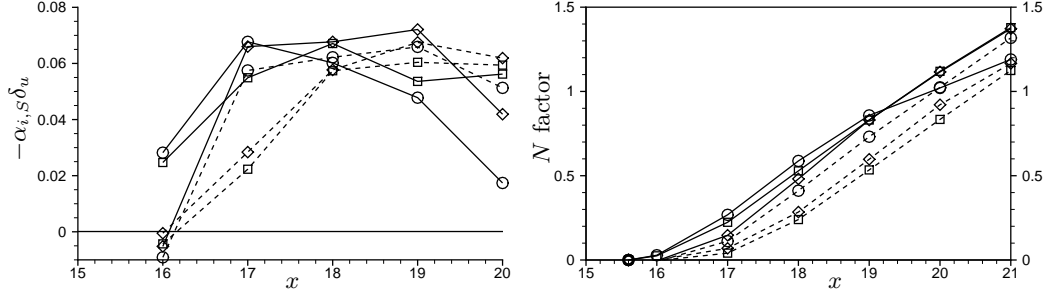


FIGURE 6. Spatial amplification rates over streamwise direction x (left) and corresponding N factors (right) for the most amplified y -mode (solid lines) and z -mode (dashed lines) at x -positions indicated by symbols. Streamwise wavenumber $\alpha_{r,S}\delta_u = \alpha_{r,t}\delta_u = 1.0$. Case I: squares, Case IIa: diamonds, Case IIb: circles.

mode they are related to the wall-normal and the spanwise gradients in the flowfield behind the roughness element, respectively.

5.3.1. Analysis along streamwise direction

The temporal approach of the stability theory requires a streamwise wavenumber to be given. As first-mode instability waves in supersonic flow over a flat plate have a wavelength of about $6\delta \leq \lambda_x \leq 10\delta$ the wavenumber is set to $\alpha_{r,t} = 5.0$, equivalently $\alpha_{r,t}\delta_u = 1.0$. Transformed spatial amplification rates $\alpha_{i,S}$ for the most amplified y - and z -mode of all three investigated cases over x are shown in Fig. 6 (left). Note that based on a fixed streamwise wavenumber, the frequency is a result of the theory and thus, may vary along x (iterations have not been performed). In the cases discussed here, it covers a range of $3.4 \leq \omega_{r,t} = \omega_{r,S} \leq 4.3$ resulting in $0.68 \leq c_{ph,t} \leq 0.86$, monotonically increasing in streamwise direction.

Considering the y -mode, it can be observed that in all cases the maximum amplification rate is of similar magnitude (Fig. 6, left), which is roughly four times the maximum primary amplification rate of the flat-plate flow at $x = 18$ ($R_x = 1341$). However, the streamwise positions of the maxima differ. The rate of Case I peaks at about $x = 18$, $15\delta_u$ behind the roughness element. While in Case IIa the maximum is moved downstream ($x = 19$, $20\delta_u$) the rate of Case IIb peaks in the near wake ($x = 17$, $10\delta_u$). Furthermore, it has to be noticed that, contrary to the other cases, Case IIa exhibits a plateau between $17 \leq x \leq 19$, holding its amplification rate at a high level near the maximum over a broader range. Downstream of $x = 19$ the amplification rates of all cases show a decay.

The z -modes are more stable than the y -modes at first, but overtake them somewhere in the interval $18 \leq x \leq 19.5$. At $x = 19$ Cases IIa and IIb show similar maximum amplification rates, about 10% higher than the maximum of Case I. Remarkably, the z -mode of Case IIb already shows high amplification in the near wake, likely owing to the stronger spanwise gradient of the primary state in this region (Fig. 4). Downstream of $x = 19$, contrary to the y -mode rates, the z -mode rates of all cases appear to persist on the same, almost-constant level up to the end of the computed domain, becoming larger than the y -mode rates. Apparently, this is consistent with the characteristics of the primary state's velocity gradients in streamwise direction (see Fig. 4). The wall-normal gradients decay while the spanwise gradients persist. Up to $x = 21$ the largest integral growth is observed for the y -mode of Cases I and IIa (Fig. 6, right). Recall that $N = \int \alpha_{i,S} dx$, and $A/A_0 = e^N$. But, assuming that the growth rates of the z -modes persist, as Fig. 6

(left) indicates, their integral growth will exceed the y -modes already slightly further downstream. Comparing the z -modes, Case IIb shows the largest growth so far owing to the comparatively high amplification rate in the near wake. We note that the analysis at streamwise stations upstream the element did not show notable amplifications.

5.3.2. Eigenfunctions

In Fig. 7 eigenfunctions of y - and z -modes of all cases are displayed corresponding to the eigenvalues found at $x = 18.0$ with a streamwise wavenumber $\alpha_{r,S}\delta_u = 1.0$. The shown modulus $u' = |\hat{u}|$ of the complex u -perturbation is normalized such that the highest value occurring in the distribution is $u' = 1.0$. The displayed modes run at a phase speed of about $0.80 \leq c_{ph,t} \leq 0.82$ in streamwise direction. The corresponding phase distribution for Case IIb is shown in the last row of Fig. 7.

The spanwise dimensions of y - or z -modes differ in the different cases. This is in accordance to the blocking width b and the angular bearing ψ of the roughness element. A larger blocking width seems to widen the amplitude distribution, compare Cases I and IIa. In contrast, the rotation by 45° reduces the width, rendering the eigenfunction more compact, which can be seen by comparing Cases I and IIb both having the same blocking width: The curvature in the near wake behind the rotated roughness element leads to a smaller spanwise distance between the inner CVP, see Fig. 2.

On the other hand, the eigenfunctions appear to be quite similar for the different cases. Only the z -mode of Case IIb shows features differing from the modes of the other cases. Here, the lateral local maxima do not bend under the center maxima toward the low-speed streak.

All shown distributions share that the maxima are located above the sonic line in the supersonic regime at the edge of the deformed boundary layer.

5.3.3. Streamwise-wavenumber dependence

In order to make sure that the most amplified modes have been found, a scan over $\alpha_{r,t}$ has been carried out at $x = 18$. The covered range is $\alpha_{r,t}\delta_u = 0.25, 0.5 - 3.0$ with a step size of 0.5 in between. Results are displayed in Fig. 8. Phase speeds vary for both modes and all cases within $0.75 \leq c_{ph,t} \leq 0.84$.

The most amplified wavenumber for the z -mode seems to be smaller than 1. The highest amplification is observed for a streamwise wavenumber of $\alpha_{r,t}\delta_u = 0.5$ corresponding to a wavelength of about $\lambda_x = 12.5\delta_u$. The maximum amplification rate of the z -modes is virtually identical for the three investigated cases. Apart from that, the curves for identical modes in Fig. 8 show similar behavior except for the y -mode of Case IIb which, compared to the y -modes of Cases I and IIa, shows a lower maximum but instead seems to be amplified over a slightly larger range of wavenumbers.

The investigated values range up to $\alpha_{r,t}\delta_u = 3.0$ associated with the second-/acoustic mode having a streamwise wavelength of about $\lambda_x = 2\delta$ in a supersonic flat-plate boundary-layer flow, but no instability was found for $\alpha_{r,t}\delta_u$ -values near 3.

5.3.4. Comparison: theory vs. unsteady DNS

For mutual validation concurrent to the theoretical stability analysis of the primary state, a disturbance calculation using spatial DNS has been set up for Case I. It was intended to compare amplification rates and disturbance amplitudes to the theoretical, temporal results. The disturbance calculation has been done with the same code that was used for the primary states (see Sec. 4). The primary-state flow has been disturbed by monofrequent 2-D blowing and suction within a spanwise disturbance strip at the

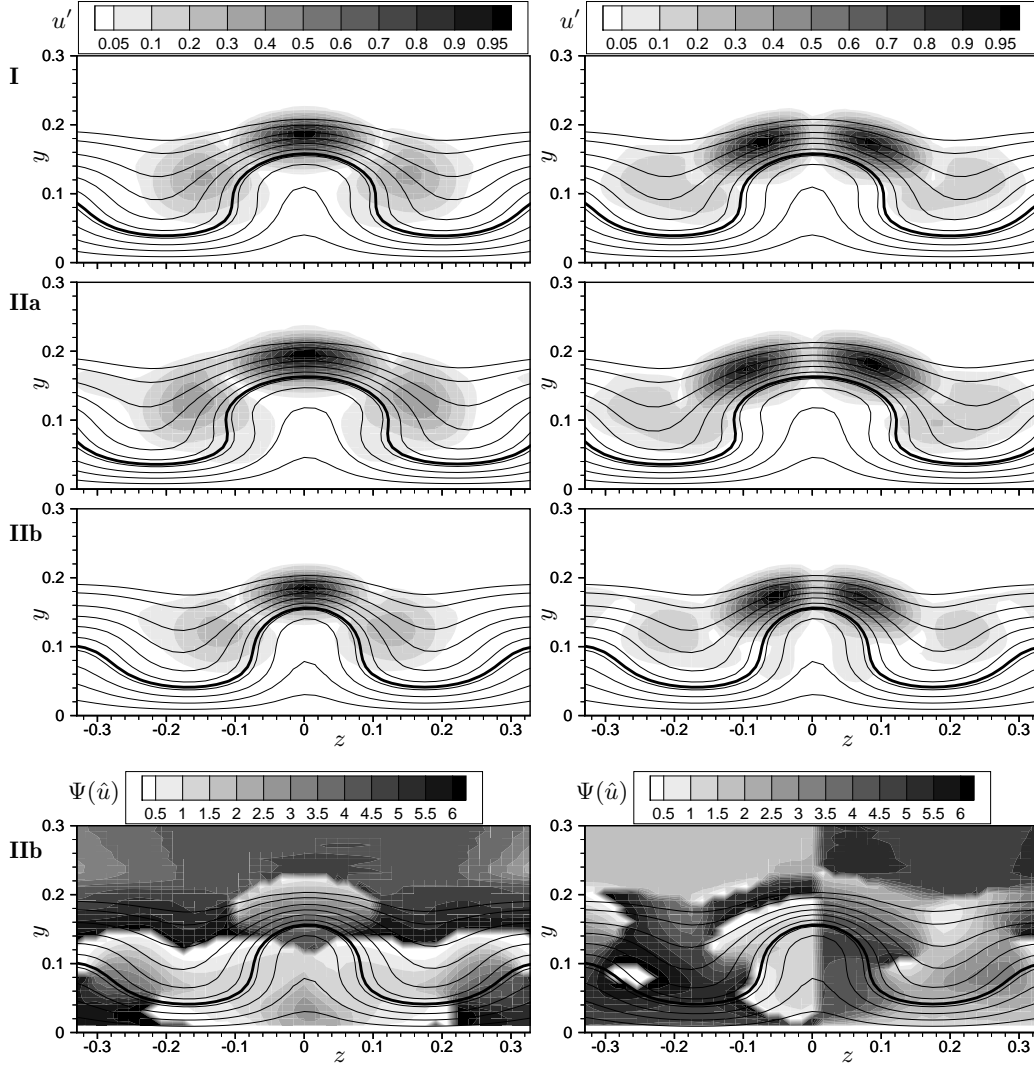


FIGURE 7. Eigenfunctions of u -velocity. Contours show the modulus of normalized u -perturbation amplitude $u' = |\hat{u}|$. y -mode (left) and z -mode (right) are displayed at position $x = 18.0$ for the three investigated cases. Thin solid lines are isolines of u beginning with $u = 0.1$ near the wall and ending with $u = 0.95$. Thick solid lines mark the sonic line. Last row: Phase distribution $\tan \Psi(\hat{u}) = \frac{u_i}{u_r}$ for the eigenfunctions of Case IIb.

wall, a short distance upstream the roughness element. The disturbance frequency is $\omega_{r,DNS} = 5.0$. Despite our awareness that disturbing a Mach 4.8 flow at the wall typically excites a sum of modes with different streamwise wavenumbers and amplification rates (see also Eissler & Bestek 1996), this methodology was chosen because it is close to what would be observed in an experiment with proven glow-discharge disturbance at the wall and the DNS code was ready for this type of disturbance.

The streamwise evolution of the maximum amplitude gained by Fourier-analysis indeed displays beatings (not shown), so a comparison of growth rates was not yet possible. [We

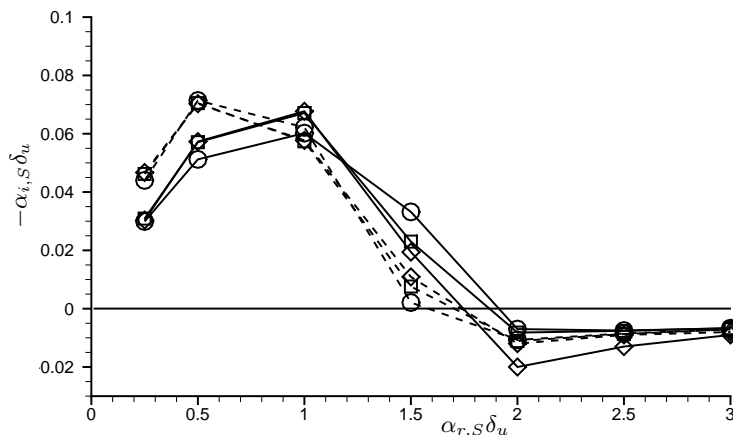


FIGURE 8. Spatial amplification rates over given streamwise wavenumbers indicated by symbols for the most amplified y -mode (solid lines) and z -mode (dashed lines) at $x = 18.0$. Case I: squares, Case IIa: diamonds, Case IIb: circles.

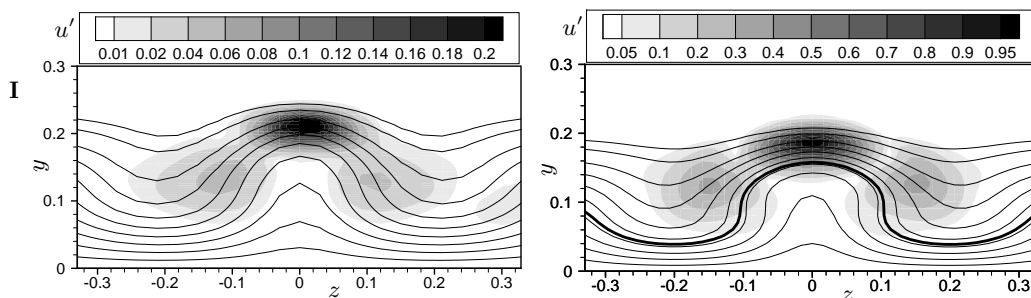


FIGURE 9. Comparison: DNS vs. theory. Left: u' -velocity perturbation amplitude u' from DNS, y -mode at position $x = 22.0$. Right: Contour of modulus of normalized u' -perturbation amplitude $u' = |\hat{u}|$ from theory, y -mode at position $x = 18.0$. Thin solid lines are isolines of u beginning with $u = 0.1$ near the wall and ending with $u = 0.95$. Thick solid lines mark the sonic line.

note that for a hypersonic case with effusion cooling, the B-SLST rates were somewhat too low.] However, near the end of the computational domain a strikingly similar y -mode, which is theoretically most amplified within the computational domain, could be found in the accompanying disturbance calculation, see Fig. 9. Note that the disturbance frequencies of both calculations differ. The temporal theory based on a fixed streamwise wavenumber yields a frequency of $\omega_{r,t} = 4.0$ for the y -mode of Case I at $x = 18.0$. Furthermore, the DNS distribution has been extracted at $x = 22$.

It was impossible to extract a clear value for the growth rate of the mode in question. Whether this behavior of the flow is due to the IBM, which is in principle unsteady to model the roughness element, is unclear. Reacting to the flow, the IBM is likely to interact with the incoming flow possibly inducing further wavenumbers to the flow, which may interfere with those created naturally by the interaction of the roughness and the 2-D disturbance.

Concerning the z -mode of Case I, it must be noted that an amplitude distribution similar to the theoretical eigenfunction could not be isolated. But following the y -mode

along x , a slight spanwise oscillation of the central amplitude maximum has been observed, which might be explained by a superposed z -mode of lower amplitude. This lower amplitude of the z -mode which, according to the theory, reaches similar amplitudes at the end of the computational domain might be traced back to a lower receptivity, an issue the stability theory does not account for.

6. Conclusions

A bi-global secondary linear stability analysis (B-SLST) and spatial DNS have been used to investigate the laminar instability caused by discrete roughness in supersonic boundary-layer flow. The pizza-box type roughness element employed is roughly 0.5 boundary-layer thicknesses high and is found not to cause sudden bypass-transition in an adiabatic Mach 4.8 flow (nor in a hot Mach 6 flow, see Birrer *et al.* 2008). Rather, the inner pair of counter-rotating vortices (CVP) past the element and the resulting low-speed streak in the downstream centerline cause a pronounced convective instability with a growth rate roughly four times the primary-instability value without roughness. The CVP has a rotation sense opposite to the outer legs of the horseshoe vortex, the latter playing virtually no role for the instability increase. The sharp, diamond-type roughness arrangement is more dangerous to laminar flow than the blunt setting where one side faces the flow. Generally, the y -mode experiences amplification only within a short range behind the roughness, with a maximum between 10 and 20 boundary-layer thicknesses past it, while the persisting amplification of the z -mode suggests this mode to be more important for transition. It also has a somewhat smaller streamwise wavenumber, that generally was found to lie near the value of one, non-dimensionalized by the boundary-layer thickness, for the most amplified modes. The comparison with an unsteady DNS showed excellent agreement of disturbance shapes, whereas the growth rates could not be directly compared yet. Of course, the theory does not account for any receptivity of disturbances that is altered by the roughness element. It remains to be checked whether the DNS providing the primary state for the stability analysis fully converges to a globally steady state.

Acknowledgements

The collaboration within the Hypersonics group as well as the climate are gratefully acknowledged. Special thanks go to Parviz Moin, Sara Bedin and Gianluca Iaccarino for the excellent setup.

REFERENCES

- BIRRER, M., STEMMER, C., GROSKOPF, G. & KLOKER, M. J. 2008 Chemical nonequilibrium effects in the wake of a boundary layer-sized object in hypersonic flows. In *Proceedings of the 2008 Summer Program*, CTR, Stanford, Calif., July 6–August 1.
- BONFIGLI, G. & KLOKER, M. J. 2007 Secondary instability of crossflow vortices: validation of the stability theory by direct numerical simulation. *J. Fluid Mech.* **583**, 229–272.

- CHOU DHARI, M. M., LI, F. & EDWARDS, J. 2008 Advanced stability analysis pertaining to roughness effects on laminar-turbulent transition in hypersonic boundary layers. *NASA AAP Quarterly Highlights* Hypersonics Project, Vol. 2, No. 2, April 2008.
- EISSLER, W. & BESTEK, H. 1996 Spatial Numerical Simulation of Linear and Weakly Nonlinear Wave Instabilities in Supersonic Boundary Layers. *Theoret. Comput. Fluid Dynamics* **8** (3), 219–235.
- KOCH, W., BERTOLOTTI, F. P., STOLTE, A. & HEIN, S. 2000 Nonlinear equilibrium solutions in a three-dimensional boundary layer and their instability. *J. Fluid Mech.* **406**, 131–174.
- LEHOUCQ, R. B., SORENSEN, D. C. & YANG, C. 1998 *ARPACK User's Guide*. SIAM, Philadelphia, Penn.
- LI, F. & CHOU DHARI, M. M. 2008 Spatially Developing Secondary Instabilities and Attachment Line Instability in Supersonic Boundary Layers. AIAA Paper 2008-590.
- LINN, J. & KLOKER, M. J. 2008 Numerical investigations of film cooling and its influence on the hypersonic boundary-layer flow. *NNFM 98*, final reviewed papers of the HGF virtual institute RESPACE Key technologies for re-usable space systems (ed. Guelhan, A.), Springer-Verlag, Berlin, 151–169.
- MALIK, M. R. & CHANG, C.-L. 1994 Crossflow disturbances in three-dimensional boundary layers: nonlinear development, wave interaction and secondary instability. *J. Fluid Mech.* **268**, 1–36.
- MARXEN, O. & IACCARINO, G. 2008 Numerical simulation of the effect of a roughness element on high-speed boundary layer instability. Thirty-eighth *AIAA Fluid Dynamics Conference & Exhibit*, 23-26 June / Seattle, Wash. AIAA Paper 2008-4400.
- MITTAL, R. & IACCARINO, G. 2005 Immersed Boundary Methods. *Ann. Rev. Fluid Mech.* **37**, 239–261.
- NAGARAJAN, S., LELE, S. K. & FERZIGER, J. H. 2003 A robust high-order method for large eddy simulation. *Physics of Fluids A* **4** (4), 710–726.
- NG, L. L. & ERLEBACHER, G. 1992 Secondary instabilities on compressible boundary layers. *J. Comput. Phys.* **191**, 392–419.
- PRUETT, C. D., NG, L. L. & ERLEBACHER, G. 1991 On the nonlinear stability of a high-speed, axisymmetric boundary layer. *Physics of Fluids A* **3** (12), 2910–2926.
- PRUETT, C. D. & ZANG, T. A. 1992 Direct Numerical Simulation of Laminar Breakdown in High-Speed, Axisymmetric Boundary Layers. AIAA Paper 1992-742.
- PRUETT, C. D., ZANG, T. A., CHANG, C.-L. & CARPENTER, M. H. 1995 Spatial Direct Numerical Simulation of High-Speed Boundary-Layer Flows Part I: Algorithmic Considerations and Validation. *Theoret. Comput. Fluid Dynamics* **7** (1), 49–76.
- VON TERZI, D. A., LINNICK, M. N., SEIDEL, J. & FASEL, H. F. 2001 Immersed Boundary Techniques for High-Order Finite-Difference Methods. Thirty-first *AIAA Fluid Dynamics Conference & Exhibit*, 11-14 June / Anaheim, Calif. AIAA Paper 2001-2918.
- WASSERMANN, P. & KLOKER, M. J. 2005 Transition mechanisms in three-dimensional boundary-layer flow with pressure-gradient changeover. *J. Fluid Mech.* **530**, 265–293.